Vascular tropism models of blood-borne microbial dissemination

Anna E. Boczula[1], Amy Ly[1], Rhodaba Ebady[1], Janet Cho[1], Zoha Anjum[1], Nataliya Zlotnikov[1], Henrik Persson[2], Tanya Odisho[1], Craig A. Simmons[2] and Tara J. Moriarty[1*]

*Corresponding author. [1]Faculties of Dentistry and Medicine (Department of Laboratory Medicine and Pathobiology), University of Toronto. 124 Edward Street Rm 555. Toronto ON, Canada M5G 1G6 tara.moriarty@utoronto.ca. Phone: 416-978-6685.

Word count: Introductory summary (255), Main text, excluding table, legends, methods (2652) References: Main text, excluding Methods & Supplemental Materials (50)

Key words: bloodborne pathogen, dissemination, Lyme disease, tropism, endothelium

Competing interests. The authors declare that the research was conducted in the absence of any commercial or financial relationships that could be construed as a potential conflict of interest The authors declare no competing interests.

Author Contributions. Conceptualization (TJM, AB, CAS), data curation (AB, TJM, AL, JC), formal analysis (AB, TJM, AL, JC, RE), funding acquisition (TJM, AB, CAS), investigation (AB, ZA, AL, RE, NZ, HP, TJM, TO, JC), methodology (AB, TJM, RE), project administration (TJM), resources (TJM, CAS), software (TJM, AB), supervision (TJM, CAS), validation (TJM, AB), visualization (AB, AL, NZ, RE), writing-original draft preparation (AB, TJM), writing- review and editing (TJM, AB, AL, JC).

1 **SUMMARY**

2 Similar to circulating tumour and immune cells, many blood-borne microbes preferentially

3 "home" to specific vascular sites and tissues during hematogenous dissemination [1–5]. For many

4 pathogens, the "postal codes" and mechanisms responsible for tissue-specific vascular tropism are

5 unknown and have been challenging to unravel. Members of the Lyme disease *Borreliella*

6 *burgdorferi* species complex infect a broad range of mammalian tissues and exhibit complex

7 strain-, species- and host-specific tissue tropism patterns. Intravenous perfusion experiments and

8 intravital microscopy studies suggest that heterogeneous tissue tropism properties may depend on

9 tissue-specific differences in host and microbial molecules supporting vascular interaction and

10 extravasation. However, interpreting these studies can be complicated because of the immune-

11 protective moonlighting (multitasking) properties of many *B. burgdorferi* adhesins. Here, we

12 investigated whether *B. burgdorferi* vascular interaction properties measured by live cell imaging

13 and particle tracking in aorta, bladder, brain, joint and skin microvascular flow chamber models

14 predict strain- and tissue-specific dissemination patterns *in vivo* These studies identified strain-

15 and endothelial cell type-specific interaction properties that accurately predicted *in vivo*

16 dissemination of *B. burgdorferi* to bladder, brain, joint and skin but not aorta, and indicated that

17 dissemination mechanisms in all of these tissues are distinct. Thus, the ability to interact with

18 vascular surfaces under physiological shear stress is a key determinant of tissue-specific tropism

19 for Lyme disease bacteria. The methods and model systems reported here will be invaluable for

20 identifying and characterizing the diverse, largely undefined molecules and mechanisms

21 supporting dissemination of Lyme disease bacteria. These methods and models may be useful for

22 studying tissue tropism and vascular dissemination mechanisms of other blood-borne microbes.

23

24 **MAIN TEXT**

25 **Generation of hTERT-immortalized primary human endothelial cells (ECs) from tissues**

26 **targeted by disseminating *B. burgdorferi*.** One barrier for flow chamber studies of bacterial-

27 endothelial cell (EC) interactions is the challenge of cultivating a sufficient number of primary

28 human ECs, which undergo replicative senescence and phenotypic drift in culture. The first goal

29 of our studies was to develop stable, replicable flow chamber models for studying bacterial-

30 endothelial interaction mechanisms. Immortalization of ECs without loss of characteristic

31 phenotypic properties has been achieved by retroviral expression of human Telomerase Reverse

1   Transcriptase (hTERT) [6]. We immortalized primary human ECs derived from umbilical vein

2   (HUVEC), aorta, bladder, brain and joint synovial microvessels by retroviral hTERT expression

3   (**Fig. 1**; **Fig. S1**). We attempted to immortalize cardiac, dermal, liver and lung microvascular ECs,

4   but found that these cell types did not grow well, quickly lost their parent morphology in culture,

5   or could not be immortalized (data not shown). hTERT expression successfully immortalized

6   HUVEC, aorta, bladder, brain and joint ECs, as determined by comparing population doubling

7   (PD) times of parental and hTERT-expressing progeny after 9-12 weeks of cultivation (**Fig. 1A**,

8   **Fig S1A**).

9   To determine if immortalized ECs retained primary EC properties we measured

10   intercellular junction expression, localization of the EC marker VE-cadherin (**Fig. 1B**, **S1B**), and

11   endothelial surface glycocalyx thickness (**Fig. 1C**) [7,8]. Immortalization reduced VE-cadherin

12   expression in aorta, bladder and joint ECs, but not HUVEC or brain ECs. (**Fig. 1B, S1B**).

13   Glycocalyx thickness measured by live cell imaging under flow was similar in parent and

14   immortalized progeny for all EC types except aorta (**Fig. 1C**), and was comparable to EC

15   glycocalyx thickness measured by cryoelectron microscopy [9].

16   Finally, we determined if immortalization affected *B. burgdorferi*-endothelial interactions

17   in flow chambers under postcapillary venule shear stress conditions at which *B. burgdorferi*-

18   vascular interactions have previously been observed (1 dyn/cm^2) [10–15]. We used three genetically

19   distinct infectious strains differing in carriage of plasmid lp25 or the gene encoding vascular

20   adhesin BBK32 (+lp25+*bbk32*, -lp25+*bbk32*, –lp25-*bbk32*) [10,11]. These strains exhibit distinct

21   dermal postcapillary venule interaction properties in live mice which are recapitulated with

22   HUVEC in flow chambers at 1 dyn/cm^2 [10–15]. We counted interactions manually and using particle-

23   tracking methods (**Fig 1D**) to capture total (bacteria moving <175 µm/sec) and slow (bacteria

24   moving <125 µm/sec) interactions for each strain and EC type. Manual counts measure the number

25   of *B. burgdorferi* moving at these velocities over EC surfaces, whereas particle tracking captures

26   numbers of binding-unbinding adhesion events that occur as bacteria move over surfaces at these

27   velocities; each bacterial interaction trajectory consists of series of binding-unbinding events [13].

28   Immortalization did not affect *B. burgdorferi*-EC interactions, measured by manual or

29   particle tracking, for EC types where VE-cadherin expression or glycocalyx thickness were

30   reduced by immortalization (p≥0.42; **Fig. S1**: aorta, bladder, joint) and for EC types where

31   immortalization did not disrupt these parameters (p≥0.19; **Fig. 1E**: brain, HUVEC). Although

2

A

B VE-cadherin (red) DAPI (blue)

C

D

E
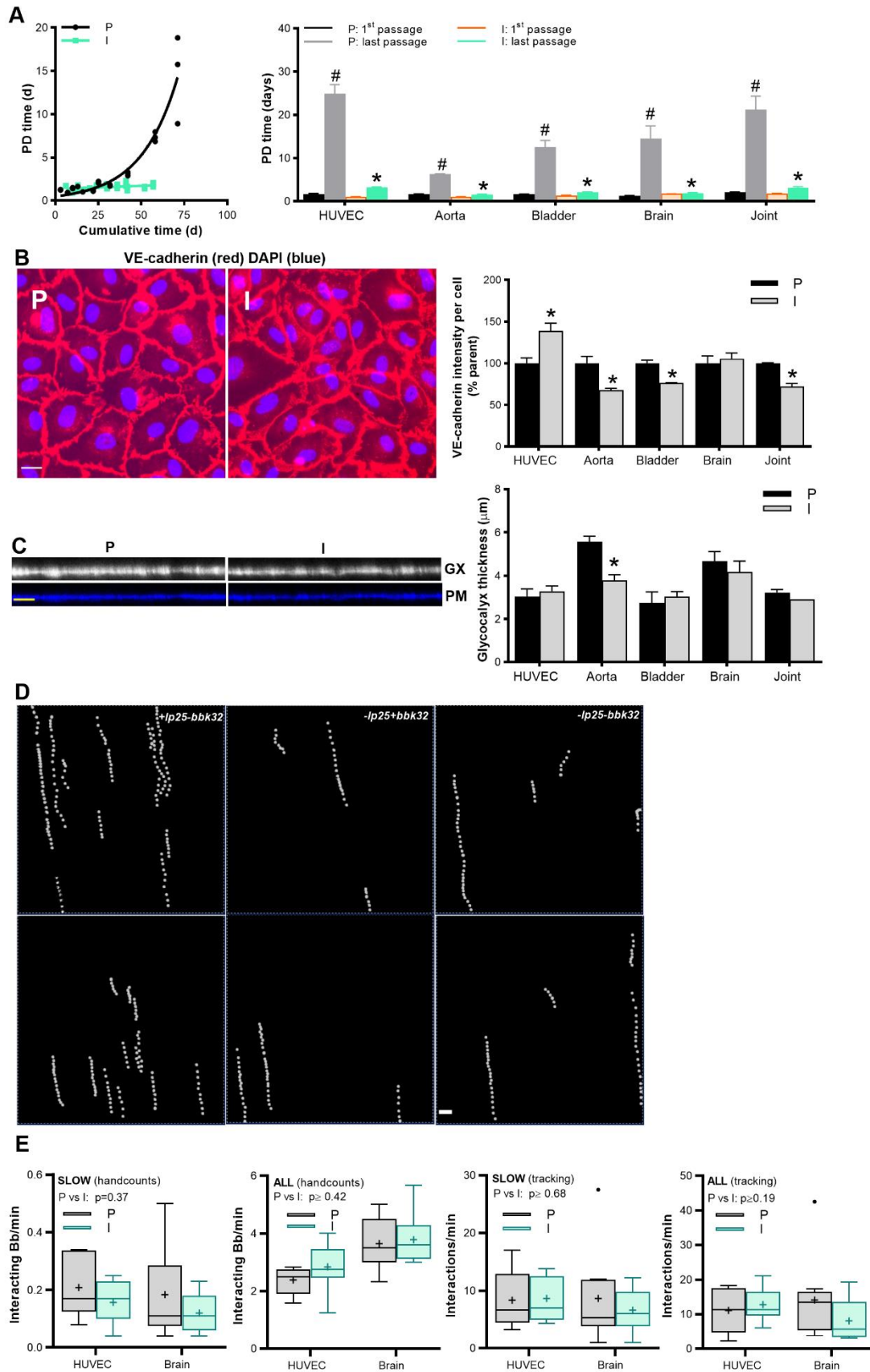
Fig 1: Generation and characterization of hTERT-immortalized primary human endothelial cells. Primary human endothelial cells (ECs) from vascular beds of indicated tissues immortalized by retrovirus-driven expression of human telomerase reverse transcriptase (hTERT). HUVEC are umbilical vein-derived ECs. **(A)** Sample non-linear regression showing change in population doubling time (PD) over time in culture for parent (P) and immortalized (I) brain microvascular ECs (left). PD plots and immunofluorescence (IF) images for other ECs are shown in **Fig. S1**. Mean ±SEM PD time at first and last passage for P and I ECs (right). **(B)** Representative epifluorescence IF photomicrographs of brain P and I ECs stained with antibody against endothelial marker VE-cadherin, and mean ±SEM VE-cadherin intensity/cell for all ECs. **(C)** Representative confocal 3D projection images of live brain ECs visualized under flow with fluorescent plasma membrane (PM) dye and wheat germ agglutinin (GX: glycocalyx), and mean ±SEM glycocalyx thickness for all ECs. **(D)** Sample 1 min time-lapse projection images of three genetically distinct bacterial strains (+lp25+*bbk32*, -lp25+*bbk32*, -lp25-*bbk32*) interacting with brain ECs under flow, captured by particle tracking. **(E)** Data are shown as Tukey box and whiskers plots of total (all) and slow (velocity <125 µm/s) interaction numbers under flow for all bacterial strains and HUVEC or brain ECs, measured by manual and particle tracking enumeration (hand counts, tracking, respectively). For all Fig. 1 experiments, N ≥ 3 independent EC and bacterial cultures. Statistics: two-way ANOVA of log-transformed values with Holm-Sidak post-tests. * indicates $p < 0.05$ P vs I (B, C, E, A: last passage). # indicates $p < 0.05$ 1st vs last passage for P or I ECs (A). Scale bars: 30 (B, C) and 20 (D) µm.
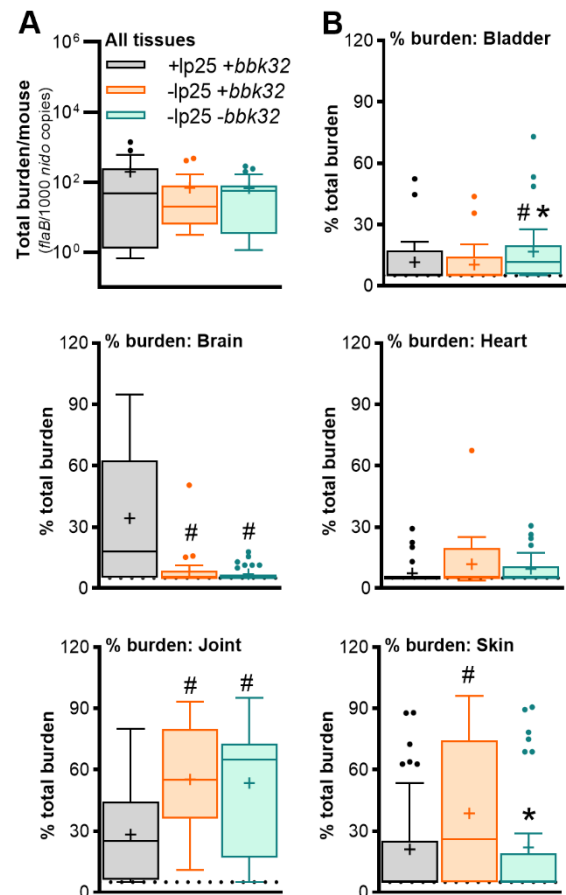
1   immortalization did not affect interaction numbers for aorta, bladder or joint ECs, we conducted

2   subsequent analyses using data only from parent ECs for these cell types to ensure that

3   unanticipated artefacts were not introduced, whereas analyses for HUVEC and brain ECs were

4   conducted with both parent and immortalized cells.

5   **Genetically distinct *B. burgdorferi* strains exhibit different tissue tropism patterns following**

6   **intravenous inoculation.** Although it seems reasonable to assume that bacterial ability to interact

7   with ECs under physiologically relevant fluid shear stress would affect their ability to disseminate

8   out of the vasculature to specific tissues (tissue tropism), this hypothesis has not been formally

9   tested. To test this hypothesis, we compared *in vitro* endothelial tropism patterns for different *B.*

10   *burgdorferi* strains to *in vivo* tropism patterns in corresponding tissues measured in *in vivo*

11   perfusion experiments (**Fig. 2, S2**). We used a short term intravenous (IV) perfusion model

12   employed previously for tissue tropism and bloodstream survival studies [16,17], but adapted this

13   model to permit inter-strain and inter-mouse comparisons independent of potential inoculation and

14   immune clearance differences among C3H/HeN mice and bacterial strains. In the original model,

15   blood is collected 1 h after inoculation of mice, followed by intracardiac saline perfusion to remove

16   unattached bacteria, and quantitative real-time PCR (qPCR) to measure bacterial burden. To

17   control for potential clearance and inoculation differences among bacterial strains and mice, we

18   expressed dissemination to each tissue in individual mice as a percentage of total dissemination to

19   all tissues measured in the same animal. Tissues examined were bladder, brain, heart, patella and

20   skin, reflecting the EC types used in flow chamber experiments. Studies were performed at one

4

hour, one day and one week after inoculation in both male and female mice to capture dissemination to all tissues independent of potential differences in dissemination kinetics, and to determine if sex affected outcomes. HUVEC has already been established as an effective model of *B. burgdorferi* murine dermal microvascular interactions [13–15]. The aorta and brain human ECs used in our studies were previously found to have similar characteristics as corresponding EC types in mice [18–22]. To the best of our knowledge, comparisons of primary bladder and joint human and mouse ECs have not been reported.

Unexpectedly, total burden across all tissues and at all timepoints was at least 1,000-fold greater in females than males (**Fig. S2A**). Although early strain specific dissemination patterns were similar in male and female mice, surprisingly we found that no strain disseminated appreciably or more than transiently to bladder or brain in female mice, whereas dissemination to heart was attenuated in male mice (**Fig. S2B**). Sex-specific *B. burgdorferi* tissue tropism patterns have not been systematically

Fig 2: Genetically distinct *B. burgdorferi* strains exhibit different tissue tropism patterns following intravenous inoculation. Total *B. burgdorferi* burden in all tissues (**A**) and percent of total burden in indicated tissues after intravenous inoculation of male mice (**B**), measured by quantitative PCR. Shown are values for all timepoints 1h, 1d, 1w. Values for individual timepoints for male and female mice are provided in Fig. S2. Data are depicted as Tukey box and whiskers plots. N≥28 mice/experimental group. Statistics: Kruskal-Wallis ANOVA of log-transformed values, with Dunn's post-tests. * indicates $p<0.05$ vs -lp25-*bbk32*. # indicates $p<0.05$ vs +lp25+*bbk32*.

investigated, although we have previously noted sex-specific differences in brain and heart burden in long-term mouse infections with the -lp25+*bbk32* strain [23]. Since we could not be certain that the dissemination patterns in females were not artefacts due to extremely high overall burdens, we conducted subsequent analysis using dissemination data from male mice (**Fig. 2**).

Consistent with earlier studies implicating BBK32 in dermal vascular interactions and dissemination to skin [10,12,13,24], BBK32-expressing strain -lp25+*bbk32* disseminated to skin more

1   efficiently than BBK32-deficient strain -lp25+*bbk32* (**Fig. 2B**). Also as observed [25], BBK32 was

2   not required for joint dissemination (**Fig. 2B**). Surprisingly, BBK32 expression in an lp25-deficient

3   background (-lp25+*bbk32*) was associated with impaired dissemination to bladder (**Fig. 2B**). As

4   reported previously for dermal postcapillary venule interactions, lp25 carriage suppressed skin

5   dissemination[10], but also suppressed dissemination to joint and promoted dissemination to brain

6   (**Fig. 2B**). No-strain specific dissemination differences were observed in heart (**Fig. 2B**).

7

8   **Bacterial-endothelial interaction numbers in flow chambers predict dissemination patterns**

9   *in vivo*. We next investigated which, if any, interaction properties measured for a specific bacterial

10 strain and human EC type in flow chambers were associated with/predictive of dissemination to

11 the corresponding murine tissue in perfusion studies (**Fig. 3, S1; Table 1**). *B. burgdorferi* interacts

12 with ECs under flow conditions through transient interactions called dragging and tethering (**Fig.**

13 **3A**), as well as by stationary adhesion [11]. Although stationary adhesion was once hypothesized to

14 be the interaction step preceding *B. burgdorferi* extravasation, extravasation has only been directly

15 observed following transient interactions [11]. We found that stationary adhesion on ECs in flow

16 chambers did not correlate with dissemination to any tissue examined (**Table 1**), implying that

17 stationary adhesion is likely not a major determinant of tissue-specific dissemination.

18   *B. burgdorferi* has a flat sine wave morphology and can interact with surfaces in flat or

19 raised orientations (**Fig. 3A**) [13,26]. Dragging *B. burgdorferi* moves slowly over EC surfaces (<125

20 µm/s) under flow, with the edge of its sine wave shape oriented perpendicular to the EC surface,

21 and forms adhesion complexes that are not stabilized by tethers (**Fig. 3A** top: -T) [13,14]. In this

22 position, mechanical load is transferred from an adhesion complex at one "sine wave peak" to an

23 adhesion complex on the next peak in the wave, and during each adhesion and load transfer event,

24 the bacteria are displaced 2.83 µm, or the distance between sine wave peaks. These interactions

25 depend on adhesion complexes that can sustain greater force on the load-bearing bond (F_b) without

26 dissociating and exhibit a smaller dissociation rate (K_{off}). By contrast, tethering bacteria are

27 oriented flat against EC surfaces under flow, displace further than 2.83 µm during each successive

28 interaction, and move faster than 125 µm/s over EC surfaces (**Fig. 3A** bottom: +T) [13,14]. Tethered

29 interactions are stabilized by as yet unidentified tethers that absorb/reduce the force imposed on

30 load-bearing adhesion complexes under flow.

31
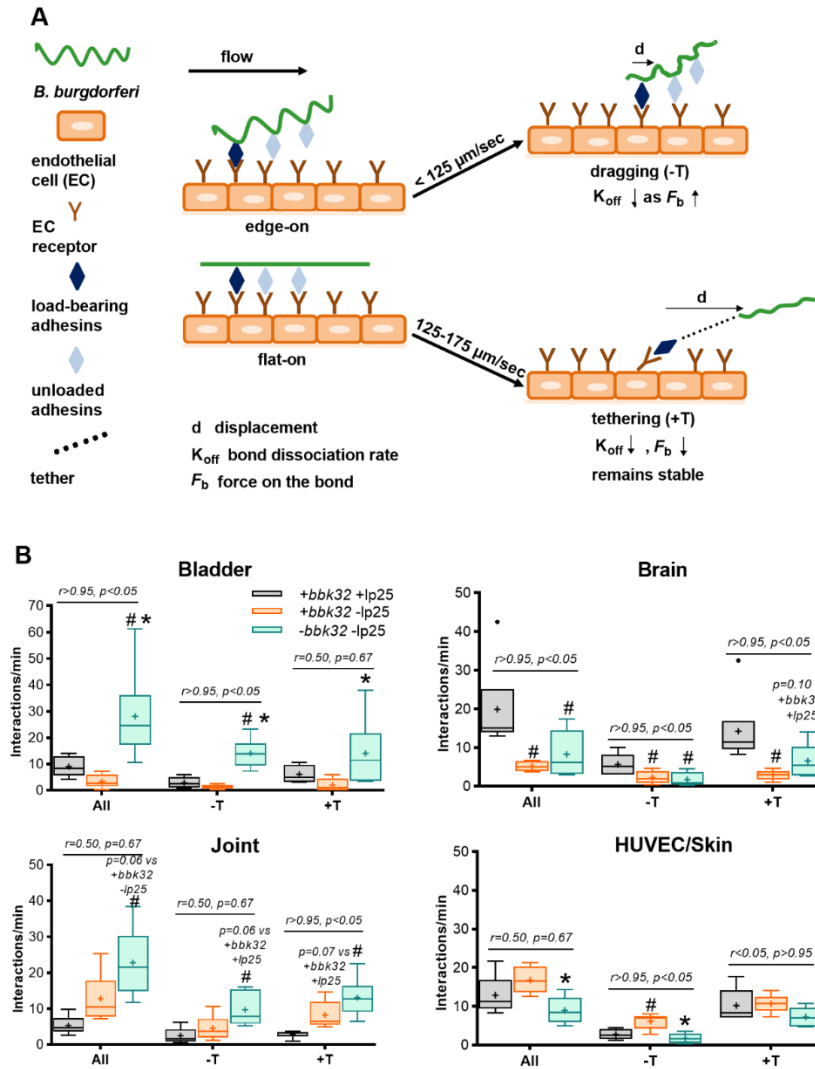
Fig. 3: Bacterial-endothelial interaction numbers in flow chambers predict dissemination patterns *in vivo*.
(**A**) Schematic depicting the two major modes of *B. burgdorferi*-EC interactions under physiological shear stress: Top: Slow, untethered (-T) "dragging" interactions in an edge-on orientation where mechanical load is transferred from peak to peak of the bacterial sine wave-shaped body (displacement, d, is wavelength), and that dissociate more slowly (K_{off}) as force on the load-bearing adhesion bond (F_b) increases. Bottom: Faster interactions in a flat orientation stabilized by tethers (+T) that slow dissociation by distributing mechanical load imposed on the adhesion bond; bacteria displace the length of the tether, which is further than peak-to-peak displacement in -T interactions. (**B**) *B. burgdorferi*-EC interaction number of interactions/min for all, -T (untethered) and +T (tethered) interactions in flow chambers, measured by particle tracking. Data shown as Tukey box and whiskers plots. N ≥3 biological replicates/experimental group. Statistical comparisons within each interaction group: ANOVA with Tukey's post-tests. * indicates $p<0.05$ vs -lp25+*bbk32*. # indicates $p<0.05$ vs +lp25+*bbk32*. Pearson correlation coefficients, *r* (strain fold differences in tissue-specific burden *in vivo* vs strain fold differences in EC-specific flow chamber interaction numbers) and correlation *p*-values are indicated above each interaction group. Correlation values for all other interaction parameters are provided in **Tables 1, S1, Fig. S3**.

1

1   To determine which, if any, interaction type or property predicted dissemination to

2   corresponding tissues *in vivo*, we manually counted numbers of dragging and tethering bacteria

3   and total interacting bacteria, and used particle tracking to identify and count total (Vel<175 All),

4   tethering (Vel<175+T, Vel 125-175) and dragging interactions (Vel<125 All, Vel<175-T) (**Table**

5   **1**). We also investigated whether other biophysical interaction properties, including velocity,

6   dissociation rate, displacement, force on the bond or number of successive interactions per

7   trajectory were associated with tissue-specific *in vivo* dissemination patterns (**Table S1**; **Fig. S3**).

8   To compare these variables, on widely different scales, to tissue burdens *in vivo*, we normalized

9   the values for each parameter to the median value of the same parameter for the -lp25-*bbk32* strain,

10   then performed correlation analysis. Since *B. burgdorferi*-HUVEC interaction properties in flow

11   chambers correspond to interaction properties measured in the skin of live mice by IVM [13–15], we

12   compared HUVEC interaction values to skin dissemination values *in vivo*. *In vivo* values used for

13   comparison were pooled from all timepoints (**Fig. 2**). No significant correlations were observed

14   for aorta ECs and heart, possibly because no significant strain differences were observed in hearts

15   of male mice *in vivo* (**Table 1**) and possibly because mouse and human aorta ECs are subjected to

16   much higher shear stress conditions *in vivo* (>10 dyn/cm^2) [27,28] than the shear stress used in our

17   studies (1 dyn/cm^2).

Table 1: Correlation analysis, tissue burden *in vivo* (male, 1h, 1d, 1w post IV injection) vs flow chamber interaction numbers

Parameter [a]	Aorta/Heart (r, p) [b]	Bladder (r, p)	Brain (r, p)	Joint (r, p)	HUVEC/Skin (r, p)
Dragging bacteria/min	n/a [c]	>0.95, <0.05	>0.95, <0.05	0.50, 0.67	>0.95, <0.05
Tethering bacteria/min	n/a	>0.95, <0.05	0.50, 0.67	>0.95, <0.05	0.50, 0.67
Total/min	n/a	>0.95, <0.05	0.50, 0.67	>0.95, <0.05	0.50, 0.67
Stationary adhesion/min	n/a	<0.05, >0.95	-0.50, 0.67	<0.05, >0.95	<0.05, >0.95
Vel<175 All	n/a	>0.95, <0.05	>0.95, <0.05	0.50, 0.67	>0.95, <0.05
Vel<175 -T	n/a	>0.95, <0.05	>0.95, <0.05	0.50, 0.67	>0.95, <0.05
Vel<175 +T	n/a	0.50, 0.67	>0.95, 0.18	>0.95, <0.05	<0.05, >0.95
Vel<125 All	n/a	>0.95, <0.05	>0.95, <0.05	0.50, 0.67	>0.95, <0.05
Vel 125-175	n/a	0.50, 0.67	>0.95, <0.05	>0.95, <0.05	-0.50, 0.67

[a] interaction parameters calculated from particle tracking data, organized by interaction type: all, -T (untethered), +T (tethered). [b] Pearson correlation coefficients, r (strain fold differences in tissue-specific burden in vivo vs strain fold differences in EC-specific flow chamber interaction numbers) and correlation p-values are indicated above each interaction group. [c] n/a: values for all strains in heart in vivo are identical (male)

18   Overall, the strongest predictors of strain- and tissue-specific dissemination patterns *in vivo*

19   were numbers of interactions measured by manual or particle tracking enumeration (**Fig. 3B,**

20   **Table 1**). Dissemination to bladder, brain and skin was associated most consistently with numbers

1   of slow (velocity <125 µm/s), untethered (-T), dragging interactions observed on bladder and

2   HUVEC ECs in flow chambers, whereas joint dissemination was associated most strongly with

3   fast (velocity >125 µm/s), tethered (+T) interactions on joint ECs (**Table 1**). Dissemination

4   patterns *in vivo* were not generally correlated with interaction velocity, dissociation rate,

5   displacement, force on the bond or number of successive interactions per trajectory (**Table 1, S1,**

6   **Fig. S3**), although it is possible that some of these properties might still be found to predict

7   dissemination if flow chamber experiments are performed over a range of shear stress conditions

8   that select for the most stable interactions [13–15].

9   These observations implied that in bladder, brain, joint and skin, dissemination out of the

10 blood stream was limited mainly by strain- and EC type-specific availability of bacterial adhesins

11 and cognate EC receptors supporting transient, dynamic adhesive interactions. That is, the rate-

12 limiting step for interactions is bond association rate. We conclude that EC interaction numbers in

13 flow chambers robustly predict dissemination to corresponding tissues *in vivo* when tissue burden

14 is adjusted for mouse- and bacterial strain-specific differences in overall burden, and that *B.*

15 *burgdorferi*-vascular interactions are likely a rate-controlling step of dissemination *in vivo*.

16

17 **Diverse tissue-specific vascular dissemination mechanisms.** Consistent with previous

18 sequencing studies of population bottlenecks during dissemination [29], we found that all strains

19 could interact with all ECs and disseminate to all tissues to some degree (**Fig. 2, 3**), implying that

20 multiple dissemination mechanisms exist for most vascular beds and tissues. *B. burgdorferi*

21 produces at least 19 surface-exposed adhesins, 17 of which have been identified as possible or

22 confirmed mediators of tissue-specific dissemination and/or colonization, and roughly half of

23 which are known or predicted to moonlight in immune evasion [3,17,30–39]. Strain- and species-

24 specific polymorphisms in several *B. burgdorferi* adhesin genes also contribute to tissue-specific

25 colonization patterns [3,40]. Thus, dissection of tissue-specific dissemination mechanisms *in vivo* can

26 be challenging. Quantitative, easily genetically and biochemically manipulated *in vitro* models

27 that eliminate confounding factors such as immune clearance and extravascular conditions

28 affecting microbe proliferation will be helpful for characterizing these mechanisms. However,

29 despite the existence of multiple dissemination mechanisms for each tissue, we found that

30 interaction/dissemination patterns for each bacterial strain, EC type and corresponding tissue were

1   different, implying that distinct primary vascular interaction mechanisms likely support

2   dissemination to each tissue (**Fig. 2, 3B**).

3   Bladder EC interactions and dissemination were lp25-independent and suppressed by

4   BBK32 (**Fig. 2, 3B**). Candidate mediators might include glycosaminoglycan- and laminin-binding

5   Lmp1 and BB0406, which have been linked to bladder in intravenous phage display and long-term

6   infectivity studies [41–45]. Since BBK32-expressing *B. burgdorferi* form a cap of polymerized plasma

7   fibronectin at the mechanical load-bearing point of contact with ECs under flow [14], it is possible

8   that BBK32 suppresses bladder dissemination by directly or indirectly blocking access of bladder-

9   specific adhesins to cognate bladder EC receptors.

10   Joint EC interactions and dissemination were BBK32-independent, as previously reported

11   [16,25], and suppressed by lp25 (**Fig. 2, 3B**). Candidate joint mediators identified previously by

12   intravenous phage display, intravital microscopy and infectivity studies include Lmp1, BB0406,

13   BB0347, OspC and VlsE, as well as P66, an integral membrane protein that mediates joint vascular

14   transmigration but not EC surface interactions [3,16,25,41,42,44,45]. These candidates bind a wide range

15   of host molecules that could potentially be involved in joint vascular interactions and

16   dissemination, including glycosaminoglycans, laminin, fibronectin, plasminogen and integrins. Of

17   particular interest is OspC, which supports transmigration out of the joint microvasculature in a

18   fashion that depends on its extracellular matrix-binding properties [3]. It is not clear how or why

19   joint EC interactions and dissemination would be suppressed by lp25, which also suppresses

20   HUVEC interactions and skin dissemination (**Fig. 2, 3B**). We examined tissue-specific

21   colonization data from the genome-wide signature-tagged mutagenesis library generated by Lin

22   and colleagues [45], and found one lp25 locus (*bbe27*) where genetic disruption appeared to increase

23   colonization of skin (ear) and joint compared to other tissues (bladder and heart) two weeks after

24   infection. The *bbe27* open reading frames encodes conserved hypothetical protein of unknown

25   function [45] that does not appear to be membrane localized (data not shown). It will be interesting

26   to determine if this locus can affect EC interactions and intravenous tissue dissemination.

27   As reported previously [10,12,13], HUVEC interactions and skin dissemination were promoted

28   by BBK32 and suppressed by lp25, but did not entirely depend on BBK32 (**Fig. 2, 3B**). Although

29   *B. garinii* DbpA/B has been found to support HUVEC interactions in flow chambers, *B.*

30   *burgdorferi* N40 DbpA/B does not [46], and the potential contributions of the *B. burgdorferi* B31

31   DbpA/B strain variant used in our studies to EC interactions and intravenous dissemination to skin

1   have not been examined. Other candidates identified in intravenous infectivity studies are BB0406,

2   P66 and the fibronectin-binding adhesin RevA [16,44].

3   Finally, we found that brain interactions and dissemination were BBK32-independent but

4   promoted by lp25 (**Fig. 2, 3B**). Lp25 encodes the glycosaminoglycan-binding adhesin BptA, which

5   is important for mouse infectivity in a tissue non-specific fashion (BptA-dependent brain

6   colonization has not been examined) [47]. Lp25 carries one additional open reading frame (*bbe09*)

7   identified as a locus important for mouse infectivity in genome-wide transposon mutagenesis

8   studies [45]. The predicted gene product is a putative membrane-localized lipoprotein, P23, that is a

9   member of the SP2/P23 conserved hypothetical protein family of unknown function [45,48]. Another

10   member of this family, the gene product of unknown function encoded by the *bbk52* locus on lp36,

11   is transcriptionally upregulated in response to mammalian host conditions by the Rrp2, RpoN and

12   RpoS regulators [49], and is transcriptionally upregulated in the central nervous system of non-

13   human primates infected with *B. burgdorferi* [50]. The potential contributions of BBE09, BBK52

14   and their encoding loci to *B. burgdorferi* pathogenesis have not yet been examined.

15   The ability to carefully dissect the molecular basis of tissue-specific vascular dissemination

16   mechanisms using *in vivo*-validated model systems will be crucial for understanding the

17   pathogenesis of *B. burgdorferi* and other blood-borne pathogens. These model systems also have

18   strong potential for discovery of novel dissemination mechanisms using sequence-tagged random

19   mutagenesis pathogen whole genome libraries and other, directed and undirected approaches.

20

21   **METHODS**

22

23   **Ethics statement.** This study was conducted in accordance with the most recent policies and Guide
24   to the Care and Use of Experimental Animals by The Canadian Council on Animal Care. Animal
25   work was approved by the University of Toronto Animal Care Committee in agreement with
26   institutional guidelines (Protocols 20009347, 20009908 and 20010430). Work with *Borrelia*
27   *burgdorferi* and primary human endothelial cells was approved by University of Toronto, Public
28   Health Agency of Canada and Canadian Food Inspection Agency guidelines (University of
29   Toronto biosafety permit 12a-M30-2).

30

31   **Mouse strains and husbandry**. Intravenous perfusion experiments were performed using 6- to 7-
32   week-old male C3H/HeN (Charles River Laboratories, Montréal, QC, Canada). Mice were housed
33   in groups of 2 to 4 per environment-enriched cage with unlimited access to water and standard
34   chow (Teklad 2018 Rodent Chow, Harlan Laboratories, Mississauga, ON, Canada).

35

36   **Primary human endothelial cell (EC) sources & cultivation.** Specific endothelial cell (EC)

types used in experiments are described in **Table S2**. All primary human ECs were purchased from Lonza (Lonza Inc. Allendale, NJ, USA) or Cell Systems (Cell Systems, Kirkland, WA, USA) and cultured at 37 °C according to the manufacturer's instructions in tissue culture-treated T75 flasks without gelatin or Fn coating, in a humidified atmosphere containing 5% CO_2. Lonza cells were cultured in EGM-2 medium (Lonza cat. CC-3156) supplemented with bullet kits CC-4147 (all cells except HUVEC) or CC-4175 (HUVEC). Cell Systems cells were initially thawed and grown for the first three passages in CSC medium supplemented with Culture Boost (Cell Systems cat. CSS-A104) and 5% heat-inactivated fetal bovine serum (FBS: Sigma-Aldrich Canada, Oakville, ON), then subsequently cultured in Lonza EGM-2 medium supplemented with bullet kit CC-4147. Cell Systems and Lonza cells were respectively frozen in Cell Freezing Medium (Cell Systems cat. 4Z0-705) or whole medium containing 1% dimethyl sulfoxide (DMSO; Bioshop Canada, Burlington, ON) and 20% heat-inactivated FBS. All ECs were passaged at ~80% confluence. Lonza cells, rinsed with 37 °C phosphate buffered saline without magnesium or calcium (PBS-/-: Multicell Wisent, St-Bruno, QC), trypsinized for 5 min at 37 °C with pre-warmed trypsin (0.05% trypsin/0.53 mM EDTA; Life Technologies Canada, Burlington, ON), followed by neutralization with complete medium. Cell Systems cells were rinsed with PRG solution (EDTA -dPBS, Cell Systems cat. 4Z0-610), trypsinized for 0.5-2 min (until rounded up but not detached) with 37 °C PRG-2 solution (Trypsin/EDTA -dPBS Solution cat. 4Z0-310), followed by neutralization with an equal volume of ice-cold PRG-3 solution (Trypsin Inhibitor-dPBS Solution cat. 4Z0-410). After trypsinization, all cells were centrifuged at 220 xg RT for 5 min followed by resuspension with fresh complete media and plated at 1:5 (Cell Systems cells)-1:10 (Lonza cells) dilutions. For all experiments only parent and immortalized ECs passaged fewer than eight times were used.

Immortalization of primary human ECs.

Retrovirus production. As previously described [51], primary ECs were immortalized by infection with retrovirus encoding hTERT, produced by transfection of Gryphon amphotropic packaging cells (Allele Biotechnology, San Diego, CA, USA) with plasmid pBABE-hygro-hTERT (cat. 1773; Addgene, Cambridge, MA, USA). Gryphon cells were cultivated according to manufacturer's instructions at 5% CO_2 37 °C in 10 cm tissue culture-treated dishes (VWR Canada, Mississauga, ON) in DMEM-high glucose (Life Technologies) supplemented with 10% heat inactivated FBS and 100 U/ml penicillin/streptomycin (Thermo Fisher Scientific Canada, Burlington, ON). Gryphon cells were grown to 50-60% confluence by plating at 3.9-5.2 x 10^6 cells/10 cm plate 18-24 h before transfection. On the day of transfection, 12 µl of FuGene HD transfection reagent (Promega, Madison, WI, USA) were added to RT serum-free Optimem medium (Fisher), followed by addition of 4 µg pBABE-hygro-hTERT prepared by maxiprep (Qiagen Canada, Mississauga, ON), to a final volume of 200 µl. This mixture was incubated for 15 min at RT, then added to Gryphon cells, followed by incubation at 32 °C/5% $C0_2$ for ~24 h, when transfection medium was replaced with 10 ml fresh complete growth medium. Retrovirus-containing supernatant was harvested at 48 and 72 h after medium change, centrifuged at 2000 xg 4 °C 5 min to pellet cell debris, filter-sterilized with a 0.22 µm filter and stored in 2 ml single-use aliquots at -80 °C.

Retroviral infection and polyclonal selection. On the day of retroviral infection of ECs, 4.6 ml of 48 h viral supernatant mixed with 14.1 µl of 8 µg/ml polybrene (Sigma) was added to 1.4-2.8 x10^6 ECs cultured to 20-30 % confluence in a T75 flask, followed by 3 h incubation at 37 °C then replacement of virus-containing medium with complete growth medium. This infection was repeated 24 h later using the 72 h viral supernatant. To select for polyclonal populations in

1   which hTERT-expressing retrovirus was stably integrated, 48 h after the last infection hygromycin
2   B (BioBasic Canada, Markham, ON) was added to endothelial cells to 20 µg/ml and included in
3   culture medium for all subsequent passages [52]. Hygromycin-resistant cells were frozen in whole
4   medium containing 1% DMSO and 20% FBS upon reaching 80% confluence and at multiple
5   passages thereafter.

6   **Measurement of population doubling (PD) times.** To determine if hygromycin-resistant
7   cells were immortal, we measured PD times of triplicate cultures of parent and hTERT-expressing
8   cells at each passage until ~2 weeks after parent cells reached replicative senescence (~2-3 months
9   total passaging time) [52]. Cells were counted at every passage (at 75-80% confluence) using a
10   Beckman coulter Z1 particle counter (Beckman Coulter Canada, Mississauga, ON), blood cell
11   counter vials (VWR) and 500 µl of a 10 ml resuspension of cells from each flask diluted with 19.5
12   ml Isoton II Diluent (Beckman). PD time, in hours, was calculated from the formula PD Time
13   (PDT) = $T*ln2/ln(Xe/Xb)$, where T is incubation time in hours. Xb and Xe are cell number at the
14   beginning and end of incubation time, respectively. PD times were converted to days and plotted
15   against cumulative days of cultivation using non-weighted least squares regression and exponential
16   growth equations fit in GraphPad Prism v. 8.4.3 (GraphPad Software, San Diego, CA, USA).

17

18   **Visualization and quantification of VE-cadherin-labelled EC junctions.** ECs grown in
19   triplicate to two days post-confluence in 48-well/9.8 mm plates (Falcon, Fisher) were rinsed with
20   37 °C PBS containing calcium and magnesium (PBS+/+: Sigma), fixed in -20 °C methanol
21   at -20 °C for 15 min, rinsed with PBS -/- (Fisher), blocked for 20 min at 37 °C in PBS-/- with 3%
22   w/v bovine serum albumin (BSA) (Sigma), incubated at 37 °C for 1 h with a 1:333 dilution of 1
23   mg/ml anti-VE-cadherin polyclonal antibody (Abcam, Toronto, ON, Canada, cat. ab33168) in
24   PBS-/- with 3% BSA, washed once with PBS-/-, blocked for 30 min at RT with 10% heat-
25   inactivated goat serum (Sigma) in PBS-/-, incubated in the dark for 1 h at RT with 5 µg/ml Alexa
26   Fluor 488-conjugated goat anti-rabbit IgG (H+L) secondary antibody (Fisher) in PBS-/- with 10%
27   goat serum, then washed three times with PBS-/-, followed by staining of cell nuclei for 3 min at
28   RT with 1 µg/ml Hoechst 33342 (Sigma) in PBS-/-, and three final rinses with PBS-/-. Samples
29   were stored in the dark at 4 °C until imaging.

30   Images were captured using an Olympus IX71 (Olympus, Tokyo, Japan) epifluorescence
31   microscope equipped with a Retiga 2000R Fast-1394 camera (QImaging, Surrey, BC, Canada), X-
32   Cite 120 series illumination source (Excelitas, Waltham, MA, US), DAPI and TXRed filters
33   (Semrock Inc., Rochester, NY,US), a 40X (NA 0.4) air objective (Olympus, Tokyo, Japan) and
34   and a custom acquisition script based on ImageJ (LOCI, University of Wisconsin, USA) [53] and
35   Micro-Manager (Vale Lab, University of California, San Francisco, CA, US) [54] software. Image
36   acquisition conditions were identical for all samples. Exposure times were 100 and 2000 ms for
37   DAPI and TXRed, respectively, with no frame averaging, 0.75X zoom, 32 bits/pixel (1200x1600
38   pixels/image, 5.53 pixels/µm) and 0.18 $µm^2$ xy pixel resolution.

39   Exported DAPI and TXRed 32-bit tiffs were converted to 8-bit in ImageJ, for all ECs,
40   TXRed signal range was set to 200-800, and DAPI signal range was set to 200-800 (brain,
41   HUVEC), 200-600 (aorta), 161-430 (bladder), 250-384 (joint).VE- cadherin signal intensity was
42   measured in the TXReD images by subtraction of average background intensity (darkest
43   10x10 $µm^2$ region of interest, ROI) from the average intensity measured in each of three 200x200
44    $µm^2$ ROIs at three distinct locations in each image. The average of background-corrected signal
45   intensity was measured per cell for the three ROIs in each image, and was expressed as a percent
46   of the average intensity for parental EC images.

1   **Visualization and quantification of EC glycocalyx thickness.** As previously described [13], ~1.6
2   x 10^5 ECs/channel were seeded in ibiTreat hydrophilic tissue-culture treated Ibidi μ-Slides VI$^{0.4}$
3   (Ibidi, Planegg, Martinsried, Germany) and cultivated to 2 d post-confluence with daily feeding (a
4   total of ~3 d). ECs were labelled for 10 min at 37 °C with 100 µl of a 1:10,000 dilution of Alexa
5   647-wheat germ agglutinin (lectin) (Life Technologies) to label the glycocalyx (GX) and for 3 min
6   with CellMask Green plasma membrane live cell imaging dye (Life Technologies) prepared in
7   endothelial growth medium to label ECs, then rinsed with perfusion medium before imaging.
8   Perfusion media containing Hank's Balanced Salt Solution (HBSS: Life Technologies), and 10 %
9   heat-inactivated FBS (Sigma) was loaded in 60 ml syringes and perfused over endothelial
10   monolayers in Ibidi chambers at 1.0 dyn/cm^2 (34.1 ml/h) using a syringe pump (Model: NE1000,
11   New Era Pump Systems Inc., Farmingdale, NY, USA). Ambient temperature on the microscope
12   stage was maintained at 28 °C using an infrared heat lamp.
13   Z-series micrographs (512x512 pixels, zoom 1.25X, xy pixel size 0.73 µm, frame average
14   10, line average 3) were collected simultaneously every 0.75 µm in bidirectional resonant mode
15   (pinhole 2.5 AU), at 511-600 nm (488 nm Argon laser, 10% intensity, HyD detector BrightR mode,
16   gain 100), and 664-721 nm (633 nm laser, 100% intensity, HyD detector standard mode, gain 100),
17   using an upright SP8 tandem scanner spectral confocal microscope equipped with a 25X 0.95 NA
18   long working range water-immersion objective and operated by LAS X v.3.1.5.16308 software
19   (Leica, Mannheim, Germany).
20   Glycocalyx thickness was measured using the line tool in Volocity v.6.5 (Quorum
21   Technologies Inc., Puslinch, ON, Canada) at each of nine positions for each micrograph (xy pixel
22   coordinates: 128x128; 128x256; 128x384; 256x128; 256x256; 256x384; 384x128; 384x256;
23   384x384), with a minimum of five independent biological replicates/experimental group. As
24   described, [55] we first identified the positions of maximum intensity in each channel on the apical
25   surface of endothelial cells. We calculated values for 25% maximum intensity, then, moving
26   apically, identified the z-position at which the intensity in each channel reached 25% of the channel
27   maximum. Glycocalyx thickness was calculated by subtracting the 25% intensity z-position in the
28   plasma membrane channel ("outer edge" of plasma membrane) from the 25% intensity z-position
29   in the glycocalyx channel ("outer edge" of glycocalyx). The median value from all nine
30   measurements from the micrograph for each biological replicate (n≥5) was used for subsequent
31   calculations and statistical analysis.
32
33   **Preparation of endothelial monolayers for flow chamber experiments.** ECs cultivated and
34   seeded on Ibidi devices as described above were labelled for 5 min at 37 °C with 100 µl of a
35   1:2,000 dilution of CellMask Orange plasma membrane live cell imaging dye (Life Technologies)
36   in endothelial growth medium, then rinsed with perfusion medium before imaging.
37
38   ***B. burgdorferi* strains and preparation of bacteria for flow chamber experiments**. All details
39   of *B. burgdorferi* strains used in this study are described previously [10–12] and in **Table S4**. As
40   reported [13] *B. burgdorferi* was grown, washed, resuspended to 4 x 10^8/ml in ice cold PBS-/-,
41   declumped, then diluted to 1 x 10^8/ml in RT HBSS containing 10% heat-inactivated FBS
42   immediately before imaging, except that bacteria were cultivated without addition of blood.
43
44   **Live time lapse imaging conditions.** Bacteria were perfused over endothelial monolayers in flow
45   chambers as described in glycocalyx imaging section. For each biological replicate (independent
46   endothelial and bacterial cultures) four 1-min xyt series (512x512, zoom 1.50X, xy pixel size

14

1   0.607 µm, line average 2) were acquired simultaneously in bidirectional resonant mode (pinhole
2   10.74 AU, frames per sec 14.08) at 497-535 nm (488 nm Argon laser, 90-98% intensity, HyD
3   detector standard mode, gain 10) and 573-790 nm (561 nm laser, 9.8% intensity, PMT detector,
4   gain 450-500) using the Leica upright SP8 tandem scanner spectral confocal microscope equipped
5   with a 25X 0.95 NA long working range water-immersion objective. Time lapse videos were
6   independently inspected by at least two individuals to confirm monolayer confluence and that at
7   least 75% of the endothelial surface was at the imaging focal plane for at least 75% of video
8   duration. Videos that did not meet these criteria were excluded from subsequent analysis.
9   Subsequent quality control and analysis steps in the time lapse bioinformatics pipeline are
10   summarized below and in **Fig. S4**.
11
12   **Manual counting of *B. burgdorferi*-endothelial interactions under flow**. Tethering (bacteria
13   that pause but move faster than 125 µm/s) and dragging (bacteria that move <125 µm/s)
14   interactions and stationary adhesions (bacteria that stay at the same position for ≥20 s) were
15   manually enumerated in time lapse videos as described [13], except that dragging was counted in
16   three 30x100 µm ROIs positioned at the centre of the field of view, and the average of this value
17   was used for subsequent analyses. Analysis to identify high certainty outlier interaction values in
18   each experimental group (typically 12-24 videos) was performed in GraphPad Prism (ROUT Q
19   0.1%). If outliers were identified in any video, it was removed from all subsequent analysis (**Fig.
20   S4**). Interaction values for each biological replicate (independent bacterial and endothelial
21   cultures) were calculated as the average of interaction values for all technical replicates (typically
22   four videos). All subsequent statistical analysis was performed with values for biological
23   replicates.
24
25   **Particle tracking and measuring physical properties of *B. burgdorferi*-endothelial
26   interactions under flow.** Leica .lif library files were imported into Volocity, acquisition frame
27   rates obtained from .lif files were entered manually, and the particle tracking was performed as
28   reported [13], with the following modifications (bioinformatics pipeline summarized in **Fig. S4**).
29   Each video was analyzed using six tracking protocols (**Table S4**), and interactions were identified
30   in the resulting trajectories using a previously described formula spreadsheet that identifies
31   individual interactions in trajectories (decelerating bacteria) and calculates physical properties of
32   these interactions (see **Table S1** for parameters). To reduce potential user error in handling
33   hundreds of thousands of lines of data from nearly 700 videos of data, macros were developed to
34   permit batch data import into this formula spreadsheet without copying and pasting (**Fig. S4**). All
35   parameter calculations and identification of untethered (-T) and tethered (+T) interactions were
36   performed as reported [13], except that for K_{off} calculations time durations for interaction populations
37   were binned in intervals of 0.07 s, and linear regressions and runs tests were performed in
38   GraphPad Prism using only interactions with durations ≤0.24 s (>95% of interactions). R^2 values
39   for all curves were ≥ 0.98 and deviation from linearity was not significant (p>0.05).
40   Deduplication (arising from identification of the same trajectory with different tracking
41   protocols) was performed by identifying interactions captured at the same time point in each video
42   and examining their centroid xy position in the field of view. Interactions in the same quadrant
43   were flagged as potential duplicates and manually verified in the original videos. Duplicate
44   flagging using centroid position alone successfully identified duplicates in >95% of cases (verified
45   by manual inspection). When duplicates were identified, the interaction where measured bacterial
46   length was longest was retained for subsequent analyses, and all other interactions were removed

1　(**Fig. S4**). After deduplication, interactions were then filtered to eliminate non-specific interactions
2　with displacement ≥45 µm, bacterial length <2.5 µm, F_b (force on the bond) < 0.113 pN, velocity
3　>175 µm/s, and trajectories with fewer than three successive interactions/track (**Fig. S4**).
4
5　**Intravenous (IV) perfusion experiments.**
6　　　　**Intravenous infection and perfusion.** These experiments were performed largely as
7　described by Caine et al. [16] Briefly, ten mice per experimental group (90 total across 9 groups)
8　were inoculated via tail vein with 1×10^8 bacteria washed twice in ice-cold PBS-/-, resuspended
9　to 1×10^9 /ml in PBS and injected using a 29-gauge needle (BD, Mississauga, ON, Canada) after
10　warming to RT. At 1 h, 1 day (24 h) or 1 week, mice were anesthetized with 1% isoflurane or 100
11　mg ketamine/kg (Rogar/STB) of body weight and 10 mg/kg xylazine (MTC Pharmaceuticals),
12　delivered by intraperitoneal injection. Anesthesia was confirmed by toe pinch, the heart was
13　exposed, and 100 µl of blood was collected using a small cut in the right atrium. A 24Gx.75in
14　catheter (BD) was inserted into the left ventricle and mice were perfused with 20 ml 0.9% sterile
15　sodium chloride (NaCl) at 4 ml/min. Successful perfusion was confirmed by blanching of tissues.
16　Whole bladder, ventral abdominal skin sections and right hemi-sections of heart, brain and patella
17　were rinsed with 1x PBS-/-, blotted dry on tissue, snap-frozen on dry ice, then stored at −80 °C.
18
19　　　　**DNA extraction and qPCR measurement of bacterial and mouse DNA copy number.**
20　Total genomic DNA was isolated from tissues using a PureLink Genomic DNA Mini Kit (Fisher)
21　and collected in 100 µl kit elution buffer. Samples for which extraction was unsuccessful were
22　excluded from further analysis. These were identified as samples with DNA concentration values
23　<10% of the median DNA concentration for the same tissue from the same experimental group
24　(<0.1% of samples). qPCR amplification of *flaB* and *nido* sequences was performed in technical
25　sextuplicate and triplicate, respectively, as described [56,57], except *nido* PCR conditions were: Step
26　1: 95 °C 5 min; Step 2: 50 cycles 98 °C 6 s, 60 °C 3 s, 68 °C 5 s; Step 3 melt curve analysis from
27　60-95 °C. Measurements with abnormal amplification curves, melting temperature or cycle
28　threshold values more than 1.5 standard deviations from the mean for each biological replicate
29　were excluded from subsequent analysis. Median *flaB* and *nido* copy number values for each
30　sample were calculated from remaining values and standard curve values obtained for serial
31　dilutions of known quantities of plasmids bearing *flaB* and *nido* sequences.
32
33　　　　**Clearance-adjusted measurement of tissue-specific dissemination.** To control for
34　potential effects of differences in bacterial clearance among experimental groups, differences in
35　tissue cellularity and resulting nido values among tissues, and differences in the lowest detectable
36　limit for *flaB*:*nido* ratios for tissues with distinct host cell densities, we calculated the median *nido*
37　value for the same tissue from all experimental groups from all experiments, and multiplied the
38　reciprocal of this value by the smallest number of *flaB* copies detectable by qPCR (0.17, or 1 copy
39　detected per six technical replicates) to obtain the zero threshold *flaB*:*nido* for each tissue. To
40　normalize the zero threshold for all tissues to the same value and adjust all *flaB*:*nido* values for
41　tissue-specific differences in cell density, we calculated the zero threshold value for each tissue
42　relative to the tissue with the lowest cell density (blood) then multiplied the *flaB*:*nido* values for
43　samples from each tissue by the normalization value for that tissue compared to blood. All
44　*flaB*:*nido* ratios for all tissues less than the universal zero threshold value (the threshold value for
45　blood) were converted to the blood zero threshold value.

16

Non-zero *flaB*:*nido* ratios that were 5-fold greater or less than 20% of the median value for the same experimental group and tissue were respectively converted to 5-fold maxima and 20% minima calculated using the median value for that group and tissue. We then calculated the sum of the *flaB*:*nido* ratios for all tissues in each mouse (referred to as "All" in **Fig. 2A**), identified mice with suboptimal tail vein injections (<10% of the median of sums of *flaB*:*nido* ratios in all tissues for each mouse in the same experimental group; <1% of all mice in all experiments), and excluded these mice from subsequent analyses.

Finally, the percentage of total bacterial burden for each mouse localized to each tissue was calculated by comparing the tissue *flaB*:*nido* ratio to the sum of *flaB*:*nido* ratios for all tissues from the same mouse. To compare experimental group effect sizes to control groups, the percent total value for the same tissue from each mouse was expressed as a fold difference compared to the median percent total value for the same tissue in control mice.

REFERENCES

1. Margraf, A., Ley, K. & Zarbock, A. Neutrophil recruitment: From model systems to tissue-specific patterns. *Trends Immunol.* **40**, 613–634 (2019).
2. Jin, X. *et al.* A metastasis map of human cancer cell lines. *Nature* **588**, 331–336 (2020).
3. Lin, Y.-P. *et al.* Strain-specific joint invasion and colonization by Lyme disease spirochetes is promoted by outer surface protein C. *PLoS Pathog.* **16**, e1008516 (2020).
4. Lamond, N. M. *et al.* Cardiotropic isolates of *Listeria monocytogenes* with enhanced vertical transmission dependent upon the bacterial surface protein InlB. *Infect Immun* **89**, e00321-20 (2021).
5. Bernabeu, M., Howard, C., Zheng, Y. & Smith, J. D. Bioengineered 3D microvessels for investigating *Plasmodium falciparum* pathogenesis. *Trends Parasitol* **S1471-4922**, 30363–9 (2021).
6. Yang, J. *et al.* Human endothelial cell life extension by telomerase expression. *J. Biol. Chem.* **274**, 26141–26148 (1999).
7. Zeng, Y., Zhang, X. F., Fu, B. M. & Tarbell, J. M. The role of endothelial surface glycocalyx in mechanosensing and transduction. *Adv. Exp. Med. Biol.* **1097**, 1–27 (2018).
8. Lampugnani, M. G., Dejana, E. & Giampietro, C. Vascular endothelial (VE)-cadherin, endothelial adherens junctions, and vascular disease. *Cold Spring Harb Perspect Biol* **10**, a029322 (2018).
9. Ebong, E. E., Macaluso, F. P., Spray, D. C. & Tarbell, J. M. Imaging the endothelial glycocalyx *in vitro* by rapid freezing/freeze substitution transmission electron microscopy. *Arterioscler. Thromb. Vasc. Biol.* **31**, 1908–1915 (2011).
10. Moriarty, T. J. *et al.* Vascular binding of a pathogen under shear force through mechanistically distinct sequential interactions with host macromolecules. *Molecular Microbiology* **86**, 1116–1131 (2012).
11. Moriarty, T. J. *et al.* Real-time high resolution 3D imaging of the Lyme disease spirochete adhering to and escaping from the vasculature of a living host. *PLoS Pathog.* **4**, e1000090 (2008).
12. Norman, M. U. *et al.* Molecular mechanisms involved in vascular interactions of the Lyme disease pathogen in a living host. *PLoS Pathog.* **4**, e1000169 (2008).

13. Ebady, R. *et al.* Biomechanics of *Borrelia burgdorferi* vascular interactions. *Cell Rep* **16**, 2593–2604 (2016).

14. Niddam, A. F. *et al.* Plasma fibronectin stabilizes *Borrelia burgdorferi*-endothelial interactions under vascular shear stress by a catch-bond mechanism. *Proc. Natl. Acad. Sci. U.S.A.* **114**, E3490–E3498 (2017).

15. Kao, W.-C. A. *et al.* Identification of Tp0751 (pallilysin) as a *Treponema pallidum* vascular adhesin by heterologous expression in the Lyme disease spirochete. *Sci Rep* **7**, 1538 (2017).

16. Caine, J. A. & Coburn, J. A short-term *Borrelia burgdorferi* infection model identifies tissue tropisms and bloodstream survival conferred by adhesion proteins. *Infect. Immun.* **83**, 3184–3194 (2015).

17. Caine, J. A. *et al. Borrelia burgdorferi* outer surface protein C (OspC) binds complement component C4b and confers bloodstream survival. *Cell. Microbiol.* **19**, e12786 (2017).

18. Shi, Y. *et al.* Publisher Correction: Rapid endothelial cytoskeletal reorganization enables early blood-brain barrier disruption and long-term ischaemic reperfusion brain injury. *Nat Commun* **11**, 4335 (2020).

19. Niego, B. *et al.* Selective inhibition of brain endothelial Rho-kinase-2 provides optimal protection of an *in vitro* blood-brain barrier from tissue-type plasminogen activator and plasmin. *PLoS One* **12**, e0177332 (2017).

20. Propson, N. E., Roy, E. R., Litvinchuk, A., Köhl, J. & Zheng, H. Endothelial C3a receptor mediates vascular inflammation and blood-brain barrier permeability during aging. *J Clin Invest* **131**, e140966 (2021).

21. Yokoyama, M. *et al.* p53 plays a crucial role in endothelial dysfunction associated with hyperglycemia and ischemia. *J Mol Cell Cardiol* **129**, 105–117 (2019).

22. Kho, J. *et al.* Argininosuccinate lyase deficiency causes an endothelial-dependent form of hypertension. *Am J Hum Genet* **103**, 276–287 (2018).

23. Zlotnikov, N. *et al.* Infection with the Lyme disease pathogen suppresses innate immunity in mice with diet-induced obesity. *Cell. Microbiol.* **19**, e12689 (2017).

24. Hyde, J. A. *et al.* Bioluminescent imaging of *Borrelia burgdorferi in vivo* demonstrates that the fibronectin-binding protein BBK32 is required for optimal infectivity. *Mol Microbiol* **82**, 99–113 (2011).

25. Kumar, D. *et al.* Intravital imaging of vascular transmigration by the Lyme spirochete: Requirement for the integrin binding residues of the *B. burgdorferi* P66 protein. *PLOS Pathog* **11**, e1005333 (2015).

26. Goldstein, S. F., Buttle, K. F. & Charon, N. W. Structural analysis of the *Leptospiraceae* and *Borrelia burgdorferi* by high-voltage electron microscopy. *J Bacteriol* **178**, 6539–45 (1996).

27. Gordon, E., Schimmel, L. & Frye, M. The importance of mechanical forces for *in vitro* endothelial cell biology. *Front Physiol* **11**, 684 (2020).

28. Feintuch, A. *et al.* Hemodynamics in the mouse aortic arch as assessed by MRI, ultrasound, and numerical modeling. *Am J Physiol Heart Circ Physiol* **292**, H884-892 (2007).

29. Troy, E. B. *et al.* Understanding barriers to *Borrelia burgdorferi* dissemination during infection using massively parallel sequencing. *Infect. Immun.* **81**, 2347–2357 (2013).

30. Caine, J. A. & Coburn, J. Multifunctional and redundant roles of *Borrelia burgdorferi* outer surface proteins in tissue adhesion, colonization, and complement evasion. *Front Immunol* **7**, 442 (2016).

31. Hyde, J. A. *Borrelia burgdorferi* keeps moving and carries on: a review of borrelial dissemination and invasion. *Front Immunol* **8**, 114 (2017).

18

32. Skare, J. T. & Garcia, B. L. Complement evasion by Lyme disease spirochetes. *Trends in Microbiology* **28**, 889–899 (2020).

33. Bernard, Q. *et al. Borrelia burgdorferi* protein interactions critical for microbial persistence in mammals. *Cell Microbiol* **21**, e12885 (2019).

34. Curtis, M. W. *et al.* Characterization of stress and innate immunity resistance of wild-type and Δp66 *Borrelia burgdorferi. Infect. Immun.* **86**, e00186-17 (2018).

35. Pietikäinen, A. *et al.* Conserved lysine residues in decorin binding proteins of *Borrelia garinii* are critical in adhesion to human brain microvascular endothelial cells. *Mol Microbiol* Online ahead of print (2021) doi:10.1111/mmi.14687.

36. Tkáčová, Z. *et al.* Identification of the proteins of *Borrelia garinii* interacting with human brain microvascular endothelial cells. *Ticks Tick Borne Dis* **11**, 101451 (2020).

37. Hahn, B. *et al.* BBB07 contributes to, but is not essential for, *Borrelia burgdorferi* infection in mice. *Microbiology (Reading)* **166**, 988–994 (2020).

38. Saputra, E. P., Trzeciakowski, J. P. & Hyde, J. A. *Borrelia burgdorferi* spatiotemporal regulation of transcriptional regulator bosR and decorin binding protein during murine infection. *Sci Rep* **10**, 12534 (2020).

39. Schlachter, S., Seshu, J., Lin, T., Norris, S. & Parveen, N. The *Borrelia burgdorferi* glycosaminoglycan binding protein Bgp in the B31 strain is not essential for infectivity despite facilitating adherence and tissue colonization. *Infect. Immun.* **86**, e00667-17 (2018).

40. Tufts, D. M. *et al.* Outer surface protein polymorphisms linked to host-spirochete association in Lyme borreliae. *Mol. Microbiol.* **111**, 868–882 (2019).

41. Antonara, S., Chafel, R. M., LaFrance, M. & Coburn, J. *Borrelia burgdorferi* adhesins identified using *in vivo* phage display. *Mol Microbiology* **66**, 262–276 (2007).

42. Yang, X., Coleman, A. S., Anguita, J. & Pal, U. A chromosomally encoded virulence factor protects the Lyme disease pathogen against host-adaptive immunity. *PLoS Pathog* **5**, e1000326 (2009).

43. Yang, X. *et al.* Middle region of the *Borrelia burgdorferi* surface-located protein 1 (Lmp1) interacts with host chondroitin-6-sulfate and independently facilitates infection. *Cell. Microbiol.* **18**, 97–110 (2016).

44. Bista, S. *et al.* A novel laminin-binding protein mediates microbial-endothelial cell interactions and facilitates dissemination of Lyme disease pathogens. *J Infect Dis* **221**, 1438–1447 (2020).

45. Lin, T. *et al.* Analysis of an ordered, comprehensive STM mutant library in infectious *Borrelia burgdorferi*: insights into the genes required for mouse infectivity. *PLoS ONE* **7**, e47532 (2012).

46. Salo, J. *et al.* Flow-tolerant adhesion of a bacterial pathogen to human endothelial cells through interaction with biglycan. *J. Infect. Dis.* **213**, 1623–1631 (2016).

47. Revel, A. T. *et al. bptA* (*bbe16*) is essential for the persistence of the Lyme disease spirochete, *Borrelia burgdorferi*, in its natural tick vector. *Proceedings of the National Academy of Sciences of the United States of America* **102**, 6972–7 (2005).

48. Purser, J. E. & Norris, S. J. Correlation between plasmid content and infectivity in *Borrelia burgdorferi. Proc Natl Acad Sci U S A* **97**, 13865–70. (2000).

49. Ouyang, Z., Blevins, J. S. & Norgard, M. V. Transcriptional interplay among the regulators Rrp2, RpoN and RpoS in *Borrelia burgdorferi. Microbiology (Reading)* **154**, 2641–2658 (2008).

50. Narasimhan, S. *et al. Borrelia burgdorferi* transcriptome in the central nervous system of non-human primates. *Proc. Natl. Acad. Sci. U.S.A.* **100**, 15953–15958 (2003).

51. Counter, C. M. *et al.* Telomerase activity is restored in human cells by ectopic expression of hTERT (hEST2), the catalytic subunit of telomerase. *Oncogene* **16**, 1217–1222 (1998).

52. Poh, M. *et al.* Blood vessels engineered from human cells. *Lancet* **365**, 2122–2124 (2005).

53. Schneider, C. A., Rasband, W. S. & Eliceiri, K. W. NIH Image to ImageJ: 25 years of image analysis. *Nat. Methods* **9**, 671–675 (2012).

54. Edelstein, A., Amodaj, N., Hoover, K., Vale, R. & Stuurman, N. Computer control of microscopes using µManager. *Curr Protoc Mol Biol* **Chapter 14**, Unit14.20 (2010).

55. Betteridge, K. B. *et al.* Sialic acids regulate microvessel permeability, revealed by novel *in vivo* studies of endothelial glycocalyx structure and function. *J. Physiol. (Lond.)* **595**, 5015–5035 (2017).

56. Javid, A. *et al.* Hyperglycemia impairs neutrophil-mediated bacterial clearance in mice infected with the Lyme disease pathogen. *PLoS ONE* **11**, e0158019 (2016).

57. Tang, T. T., Zhang, L., Bansal, A., Grynpas, M. & Moriarty, T. J. The Lyme disease pathogen *Borrelia burgdorferi* infects murine bone and induces trabecular bone loss. *Infect. Immun.* **85**, e00781-16 (2017).

SUPPLEMENTAL TABLES

Table S1: Correlation analysis: tissue burden *in vivo* vs flow chamber interaction parameters, 1 h, 1 d, 1 w post-IV inoculation

Parameter [a]	*Bladder* (r, p) [b]	*Brain* (r, p)	*Joint* (r, p)	*HUVEC/Skin* (r, p)
Interaction Velocity <175: ALL				
Velocity (µm/sec)	<0.05, >0.95	0.50, 0.67	0.50, 0.67	**>0.95, <0.05**
K_{off} *(s^-1)*	0.50, 0.67	0.50, 0.67	<0.05, >0.95	<0.05, >0.95
Displacement (µm)	**>-0.95, <0.05**	0.50, 0.67	0.50, 0.67	<0.05, >0.95
F_b *(pN)*	<0.05, >0.95	<0.05, >0.95	<0.05, >0.95	<0.05, >0.95
Interactions/track	**>0.95, <0.05**	<0.05, >0.95	<0.05, >0.95	<0.05, >0.95
Velocity <175: -T				
Velocity (µm/sec)	0.50, 0.67	0.50, 0.67	<0.05, >0.95	<0.05, >0.95
K_{off} *(s^-1)*	0.50, 0.67	0.50, 0.67	<0.05, >0.95	-0.50, 0.67
Displacement (µm)	<0.05, >0.95	0.50, 0.67	<0.05, >0.95	<0.05, >0.95
F_b *(pN)*	<0.05, >0.95	<0.05, >0.95	<0.05, >0.95	<0.05, >0.95
Interactions/track	**>0.95, <0.05**	0.50, 0.67	<0.05, >0.95	<0.05, >0.95
Velocity <175: +T				
Velocity (µm/sec)	<0.05, >0.95	0.50, 0.67	0.50, 0.67	<0.05, >0.95
K_{off} *(s^-1)*	<0.05, >0.95	<0.05, >0.95	<0.05, >0.95	<0.05, >0.95
Displacement (µm)	**>0.95, <0.05**	**>0.95, <0.05**	0.50, 0.67	<0.05, >0.95
F_b *(pN))*	<0.05, >0.95	0.50, 0.67	<0.05, >0.95	**>0.95, <0.05**
Interactions/track	0.50, 0.67	0.50, 0.67	<0.05, >0.95	<0.05, >0.95

[a] *interaction parameters calculated from particle tracking data, organized by interaction type: all, -T (untethered), +T (tethered).*
[b] *Pearson correlation coefficients, r (strain fold differences in tissue-specific burden in vivo vs strain fold differences in EC-specific flow chamber interaction numbers) and correlation p-values are indicated above each interaction group.*

Table S2: Primary human endothelial cell types used in this study

Vascular bed	*Cell Type*	*Abbreviation*	*Single or multiple donors* [a]	*Sex*	*Source*	*Catalog number*
Aorta	arterial	HAEC	single	female	Lonza Inc	CC-2535
Bladder	microvascular	HMVEC- Bd	single	female	Lonza Inc	CC-7016
Brain cortex	microvascular	HMVEC-Br	single	male	Cell Systems	ACBRI 376
Synovial tissue	microvascular	HMVEC-Joint	single	female	Cell Systems	ACBRI 488
Umbilical cord vein	venous	HUVEC	multiple	female	Lonza Inc	CC-2519

[a] *all endothelia were derived from healthy donors.*

**Table S3: *B. burgdorferi* strains used in this study**

Strain	*Background*	*Description*	*Antibiotic resistance* [a]	*No flow bacterial length (µm)* [b]	*References*
GCB726 (+lp25 -bbk32)	B31 5A4 NP1	infectious B31 5A4 NP1 derivative expressing P_{flaB} -driven GFP; contains all endogenous plasmids except cp9	gentamicin, kanamycin	15.40	[11]
GCB966 (-lp25 +bbk32)	B31 ML23 derivative (ML23/pJW201)	infectious ML23-derived strain expressing P_{flaB} -driven GFP; lacks lp25; *bbe22* locus carried on plasmid pJW201(P_{flaB}-GFP/bbe22)	gentamicin	14.85	[10]
GCB971 (-lp25 -bbk32)	B31 ML23 derivative (JS315/pJW201)	ML23-derived *bbk32:strR* strain expressing P_{flaB} -driven GFP; isogenic parent: GCB9666	gentamicin, streptomycin	13.31	[10]

[a] *Antibiotic concentrations: gentamicin (100 µg/ml), kanamycin (200 µg/ml), streptomycin (50 µg/ml).* [b] *This study. Average length of single (unreplicated) bacteria for indicated strains, measured by life cell imaging in flow chambers and particle tracking of time lapses acquired using the Leica microscope under no flow conditions.*

Table S4: Particle tracking conditions

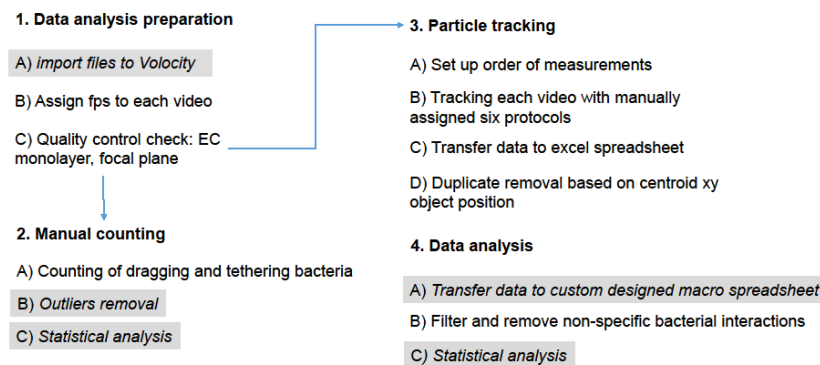| Protocol	Parameters	GCB726	GCB966	GCB971
A	**Object size** (μm^2): 1.5-1.1X no-flow bacterial length (BL)	1.5-16.95	1.5-16.33	1.5-14.64
	Object Skeletal length (μm): 2.5-1X BL	2.5- 15.4	2.5- 14.85	2.5- 13.31
	Object Intensity	17-255		
	Object joining (tracking) algorithm	Trajectory Variation (0.01), Estimate Max Distance between Objects Automatically		
	Maximum Track Velocity ($\mu m/s$)	300		
B	**Object size** (μm^2): 1.5-1.1X no-flow bacterial length (BL)	1.2-53.28	1.2-51.38	1.2-46.05
	Object Skeletal length (μm): 2.5-1X BL	1.4-15.4	1.4-14.85	1.4-13.31
	Object Intensity	40-135		
	Object joining (tracking) algorithm	See details above in protocol A		
	Maximum Track Velocity ($\mu m/s$)	$\leq$185 $\mu m/sec$		
C	**Object size** (μm^2): 1.5-1.1X no-flow bacterial length (BL)	5.0-53.28	5.0-51.38	5.0-46.05
	Object Skeletal length (μm): 2.5-1X BL	1.4-15.4	1.4-14.85	1.4-13.31
	Object Intensity	40-135		
	Object joining (tracking) algorithm	See details above in protocol A		
	Maximum Track Velocity ($\mu m/s$)	$\leq$300 $\mu m/sec$		
D	**Object size** (μm^2): 1.5-1.1X no-flow bacterial length (BL)	1.2-53.28	1.2-51.38	1.2-46.05
	Object Skeletal length (μm): 2.5-1X BL	1.4-15.4	1.4-14.85	1.4-13.31
	Object Intensity	110-255		
	Object joining (tracking) algorithm	See details above in protocol A		
	Maximum Track Velocity ($\mu m/s$)	$\leq$185 $\mu m/sec$		
E	**Object size** (μm^2): 1.5-1.1X no-flow bacterial length (BL)	5.0-53.28	5.0-51.38	5.0-46.05
	Object Skeletal length (μm): 2.5-1X BL	1.4-15.4	1.4-14.85	1.4-13.31
	Object Intensity	110-255		
	Object joining (tracking) algorithm	See details above in protocol A		
	Maximum Track Velocity ($\mu m/s$)	$\leq$300 $\mu m/sec$		
F	**Object size** (μm^2): 1.5-1.1X no-flow bacterial length (BL)	1.5-16.95	1.5-16.33	1.5-14.64
	Object Skeletal length (μm): 1.4-1X BL	1.4-15.4	1.4-14.85	1.4-13.31
	Object Intensity	17-255		
	Object joining (tracking) algorithm	Shortest Path (Max Distance 15 μm)		
	Maximum Track Velocity ($\mu m/s$)	200		

SUPPLEMENTAL FIGURES
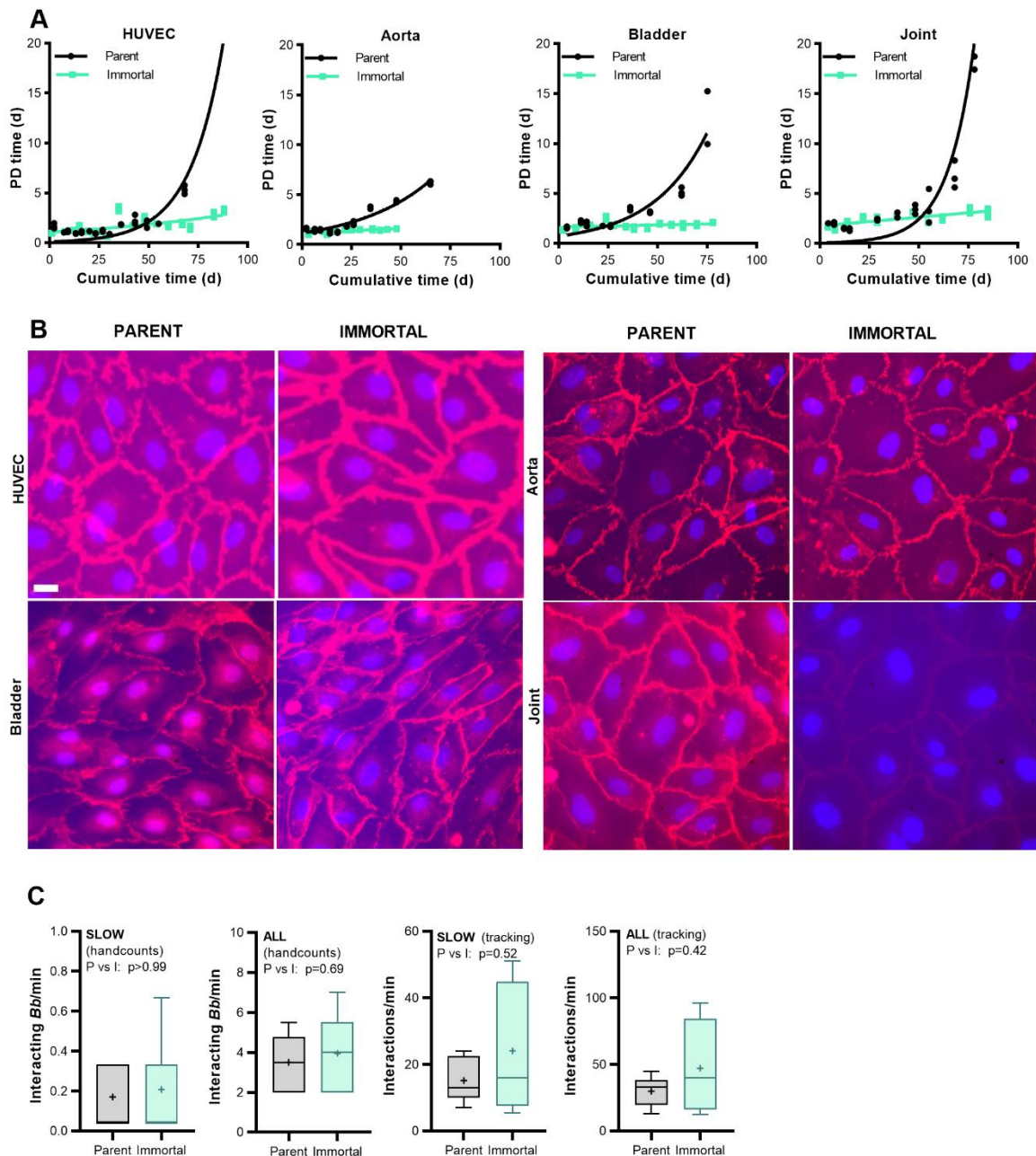
Fig S1: Population doubling times and VE-cadherin expression in parent and immortalized ECs. (A) Population doubling (PD) time plots and non-linear regressions for parent (P) and hTERT-immortalized (I) ECs. **(B)** IF visualization of VE-cadherin (red) in P and I ECs counterstained with DAPI (blue). Scale bar: 30 µm. **(C)** Data are shown as Tukey box and whiskers plots of total (all) and slow (velocity <125 µm/s) interaction numbers under flow for all bacterial strains (+lp25+*bbk32,* -lp25+*bbk32,* -lp25-*bbk32*) and ECs derived from aorta, bladder and joint, measured by manual and particle tracking enumeration (hand counts, tracking, respectively). For all Fig. S1 experiments, N ≥ 3 independent EC and bacterial cultures. Statistics: Mann-Whitney or Welch's t-test (depending on normality of distribution, determined by normality tests) of log-transformed data.

23
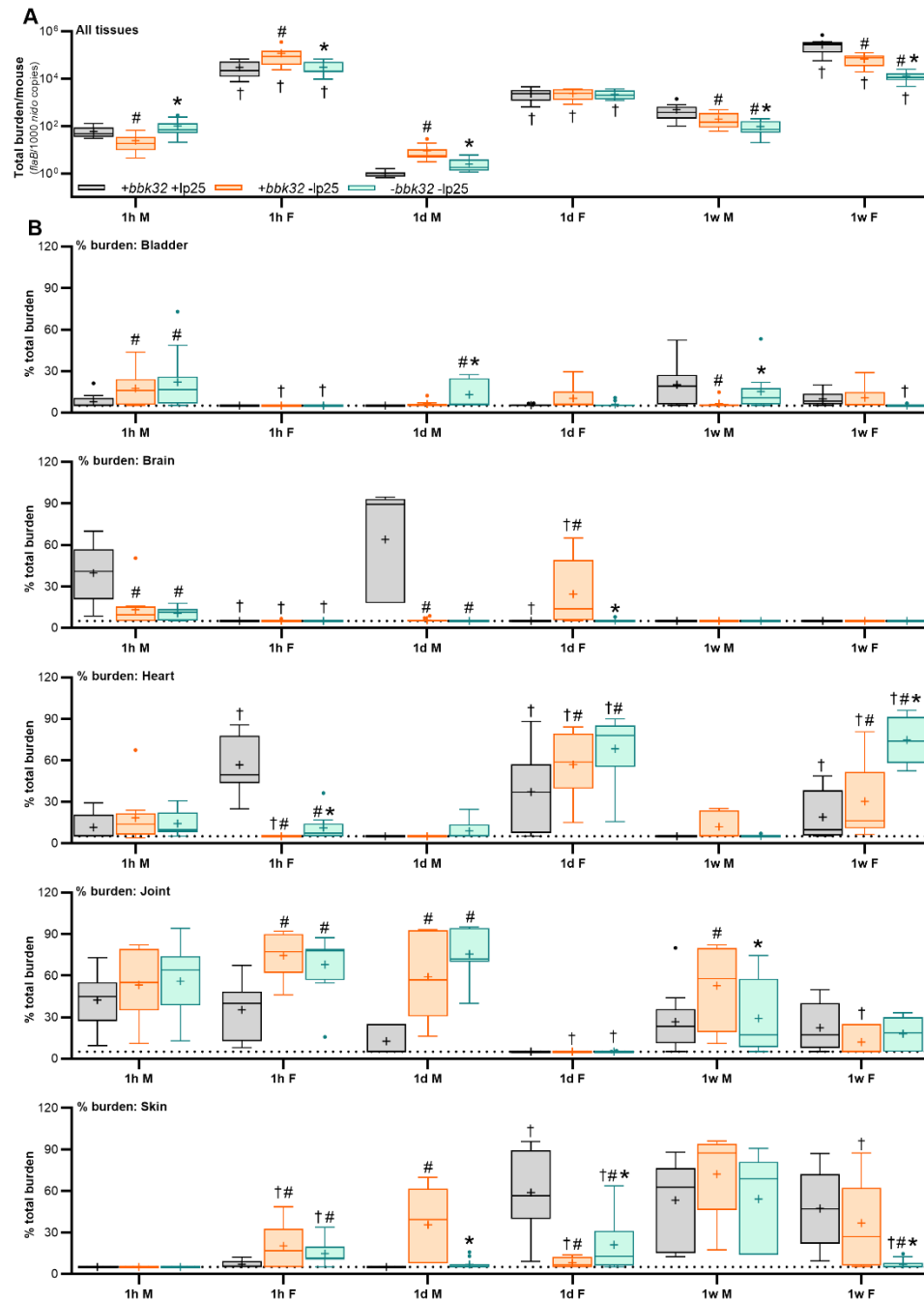
Fig. S2: *B. burgdorferi* **dissemination to tissues after intravenous inoculation of male or female mice.** Total *B. burgdorferi* burden in all tissues **(A)** and percent of total burden in indicated tissues at 1 h, 1day (d) and 1 week (w) after intravenous inoculation of female and male mice **(B)**, measured by quantitative PCR. Data are shown as Tukey box and whiskers plots. N≥26 mice/experimental group. Statistics: two-way ANOVA of log-transformed values, with Holm-Sidak post-tests. * indicates p<0.05 vs -lp25-*bbk32*. # indicates p<0.05 vs +lp25+*bbk32*.

24
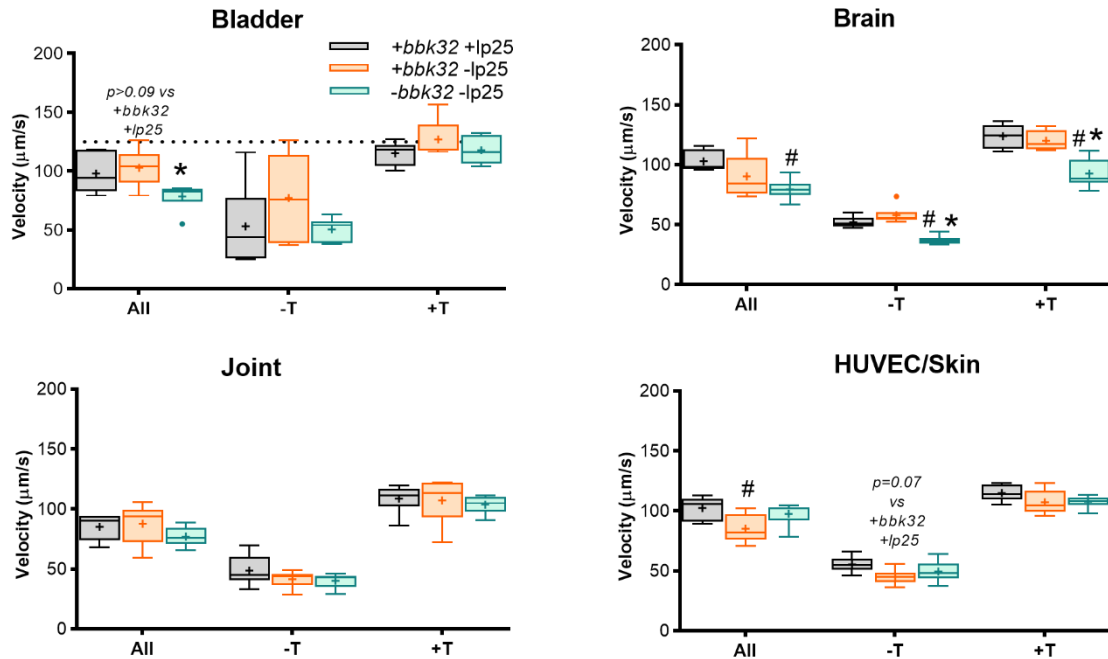
Fig. S3: Bacterial-endothelial interaction velocity in flow chambers predict dissemination patterns *in vivo*. *B. burgdorferi*-EC interaction velocity (µm/s:) for all, -T (untethered) and +T (tethered) interactions in flow chambers, measured by particle tracking. Data shown as Tukey box and whiskers plots. N ≥3 biological replicates/experimental group. Statistical comparisons within each interaction group: ANOVA with Tukey's post-tests. * indicates $p<0.05$ vs -lp25+*bbk32*. # indicates $p<0.05$ vs +lp25+*bbk32*. Pearson correlation coefficients, *r* (strain fold differences in tissue-specific burden *in vivo* vs strain fold differences in EC-specific flow chamber interaction numbers) and correlation *p*-values are indicated above each interaction group. Correlation values for all other interaction parameters are provided in **Tables 1 and S1.**

Fig. S4: Bioinformatics summary of particle tracking and measuring biophysical properties of *B. burgdorferi*-endothelial interactions under flow. Quality control and analysis steps in the time lapse bioinformatics. Highlighted in grey are steps performed using automated spreadsheets and software (Volocity, GraphPad Prism). Other steps are performed manually.